PAPER

Check for updates

Tunable insulator–metal transition in epitaxial VO$_2$ thin films *via* strain and defect engineering†

Aditya Kamat, [a] Gurukrishna K., [a] Rishow Kumar,[a] Abhishek Mishra,[b] Amit Kumar Verma,[b] Shivam Tripathi,[a] Ashish Garg[c] and Shikhar Misra *[a]

The Metal to Insulator Transition (MIT) in materials, particularly vanadium dioxide (VO$_2$), has garnered significant research interest due to its potential applications in smart windows, memristors, transistors, sensors, and optical switches. The transition from an insulating, monoclinic phase to a conducting, tetragonal phase involves changes in optical and electrical properties, opening avenues in adaptive radiative coolers, optical memories, photodetectors, and optical switches. VO$_2$ exhibits MIT close to 68 °C, thereby requiring tuneable transition temperatures (T_c) in VO$_2$ thin films for practical device applications. In this work, we explore the role of strain and defect engineering in tuning the MIT temperature in epitaxial VO$_2$ thin films deposited on *c*-cut sapphire using Pulsed Laser Deposition (PLD). The study involves tuning the metal-to-insulator transition (MIT) by varying growth parameters, mainly temperature and oxygen partial pressure. Strain engineering along the *b*-axis helped tune the transition temperature from 65 °C to 82 °C with the out-of-plane *b*-strain varying from −0.71% to −0.44%. Comprehensive structural and property analyses, including X-ray diffraction (XRD), Reciprocal Space Mapping (RSM), X-ray Photoelectron Spectroscopy (XPS), Raman spectroscopy, and resistivity–temperature (R–T) measurements, were performed to correlate structural properties with T_c. Additionally, density functional theory (DFT) calculations were performed using Quantum Espresso within the generalized gradient approximation of the revised Perdew–Burke–Ernzerhof (PBEsol) functional to provide theoretical validity to the experimentally obtained results. Our study provides critical insights into the interplay between strain and oxygen vacancies and their effect on the physical properties of VO$_2$ thin films with DFT calculations supporting the experimental findings.

Introduction

Metal to Insulator Transition (MIT) has been a hot topic amongst researchers in the recent past owing to its potential in applications such as smart windows, memristors, transistors, sensors and optical switches.[1–4] A material which exhibits MIT can transform from an insulating, transparent low temperature phase to a conducting, opaque high temperature phase with application of sufficient energy to trigger the transition. Vanadium dioxide (VO$_2$) in particular has been a subject of interest due to its metal-to-insulator transition temperature (T_c) at approximately 68 °C, a value very close to room temperature compared with the other alternatives.[5,6] With increasing temperature, VO$_2$ transitions from high resistance, transparent,

monoclinic $P2_1/c$ to low resistance, opaque, tetragonal $P4_2/mnm$.[7–9] This is accompanied by a change in optical and electrical properties (optical changes being visible in the IR region), thereby leading to exciting applications in optical devices including adaptive radiative coolers, optical memories, photodetectors, and optical switches.[5,10,11]

However, for application in practical devices, tuneable T_c in VO$_2$ thin films is required for different operating conditions. This has been mainly achieved through strain engineering and elemental doping in the past.[12] Recent studies have demonstrated the tuneable T_c in VO$_2$ by using different substrates.[13] For example, T_c of 340 K and 292 K has been obtained, when epitaxial VO$_2$ films were deposited on (0006) Al$_2$O$_3$ and (001) TiO$_2$ substrates, respectively.[14,15] VO$_2$-based nanocomposites deposited on *c*-cut sapphire have also shown a bidirectional T_c tuning from 323.5 K (Au–VO$_2$ nanocomposite) and 366.7 K (Pt–VO$_2$ nanocomposite), compared to a T_c of 344 K, which was obtained for pure VO$_2$ on *c*-cut sapphire.[16,17] Studies have also reported an increase in T_c for higher substrate deposition temperatures, consequently as a way of changing the size of gold nanoparticles embedded within the VO$_2$ matrix.[17] Similar reports have been published on nanocomposites of VO$_2$

aDepartment of Materials Science and Engineering, Indian Institute of Technology Kanpur, Kalyanpur, Kanpur, India 208016. E-mail: shikharm@iitk.ac.in

bDepartment of Electrical Engineering, Indian Institute of Technology Kanpur, Kalyanpur, Kanpur, India 208016

cDepartment of Sustainable Energy Engineering, Indian Institute of Technology Kanpur, Kalyanpur, Kanpur, India 208016

† Electronic supplementary information (ESI) available. See DOI: https://doi.org/10.1039/d4na00682h

embedded with platinum, nickel and tungsten.[18–20] Yang *et al.* fabricated a VO_2–Nb:TiO_2 heterojunction whose optical properties were studied with respect to thermally actuated MIT.[21] Moatti *et al.* studied the effect of oxygen vacancies introduced *via* vacuum annealing on VO_2/NiO/*c*-Al_2O_3 heterostructures.[22] However, limited research has been done on the role of oxygen vacancies introduced directly by changing the partial pressure of oxygen inside the deposition chamber. Since oxygen vacancies are positively charged in nature, they act as conducting channels which stabilize the conducting, high temperature phase and therefore bring T_c closer to room temperature. Studies have shown that increasing the oxygen partial pressure during growth reduces the *b*-axis spacing up to a certain limit.[23,24] A further increase in oxygen flow rate results in an increase in the *b*-axis lattice parameter of the (020) VO_2 on (0006) sapphire which might be due to the lack of opportunities for the oxygen ions to diffuse into the VO_2 surface.[24] Some review reports have discussed how the oxygen vacancies influence the transition temperature.[5,10] Fan *et al.* studied the role of vacancies in the growth of VO_2 films on MgF_2 substrates by rf-plasma assisted MBE.[25] Koussi *et al.* studied the effect of oxygen vacancies introduced by post-deposition rapid thermal annealing (RTA).[26] Lu *et al.* studied the role of vacancies formed at the grain boundaries in VO_2 growth on Pt-coated silicon substrates.[27] However, study of the correlation between the role of oxygen vacancies and change in lattice strain using structural and electrical characterization, especially for epitaxial VO_2 films grown on *c*-sapphire has been very limited. In addition, limited computational studies have been performed on the phase stability of strained epitaxial VO_2 thin films, which can provide critical insights into strain engineering for obtaining tuneable MIT.

In this work, we have explored the effect of oxygen vacancies and strain in epitaxial VO_2 thin films deposited on *c*-cut sapphire using Pulsed Laser Deposition (PLD) as shown schematically in Fig. 1(d). This was enabled by varying the deposition parameters, including the deposition temperature and oxygen partial pressure, giving rise to tuneable T_c. Detailed structural and property analyses including X-ray diffraction (XRD), Reciprocal Space Mapping (RSM), X-ray Photoelectron Spectroscopy (XPS), Raman spectroscopy, and resistivity–temperature (R–T) measurements were conducted to correlate the structural properties with the tuneable T_c. In addition, DFT calculations were also performed to study the effect of strain on the phase stability and the transition temperature.

Methodology

Thin film growth

VO_2 thin films were deposited on a *c*-cut sapphire substrate using a Coherent COMPex Pro laser system (248 nm KrF excimer laser). Prior to the deposition, the substrates were cleaned using an ultra-sonicator for 20 minutes each in acetone, ethyl alcohol and deionized water respectively, in that sequence, followed by dry blowing in N_2. The base pressure of the chamber was 3.5×10^{-6} mbar (2.625×10^{-6} Torr) or lower before deposition. A frequency of 5 Hz and laser fluence of 2.5 J cm^{-2} were used for all the depositions. The depositions were carried out at three different substrate temperatures (550 °C, 600 °C and 650 °C), and three different oxygen pressures (2.5 mTorr, 5 mTorr, and
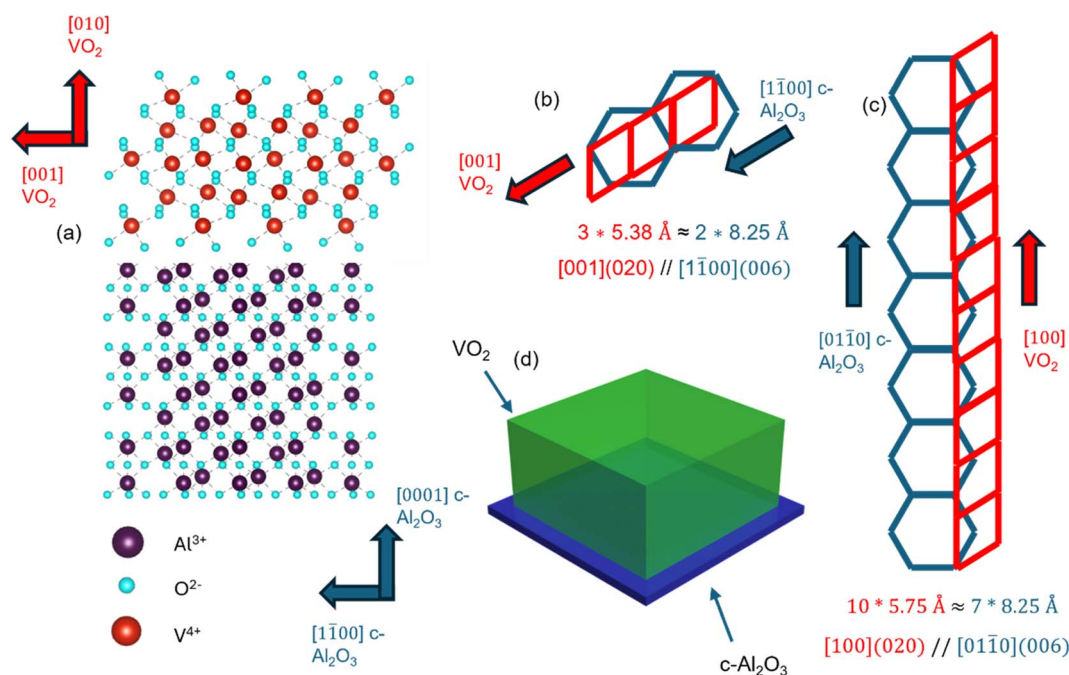

Fig. 1 Schematics of the VO_2 thin film stack on (0001) Al_2O_3 showing an epitaxial relationship. (a) Cross sectional view of the stack; (b) 3 : 2 domain matching epitaxy of (020) VO_2 along [001] deposited on (0001) Al_2O_3 along [1$\bar{1}$00]; (c) 10 : 7 domain matching epitaxy of (020) VO_2 along [100] deposited on (0001) Al_2O_3 along [01$\bar{1}$0]; (d) a 3D schematic of the VO_2 thin film deposited on *c*-Al_2O_3.

7.5 mTorr). After depositions were completed, the films were annealed for 30 minutes, followed by cooling to 25 °C in 30 minutes.

Structural and property characterization

A Malvern Panalytical Empyrean was used for X-Ray Diffraction (XRD), in which high resolution XRD scans were performed in thin film mode for step size of 0.004° and scan rate of 0.6 s per degree. Confocal Raman spectroscopy was performed using an Acton Spectrapro 2500i spectrometer from Princeton Instruments to further characterize the samples. All the samples were excited with a laser wavelength of 532 nm with 40 mW power. The data was accumulated twenty times, with exposure time of 2 s. UV-vis-NIR spectroscopy was used to measure the film reflectance in a 250–1500 nm wavelength range using a Jasco V-770 spectrophotometer in reflectance mode. XPS scans were performed using a PHI 5000 Versa Probe II from FEI Inc., utilizing an X-ray of diameter 100 μm from a 100 W power source. The scans were performed from 0 to 1200 eV for all the samples, with a resolution of 0.8 eV at a vacuum of 10^{-7} mbar to confirm the quantity of each element (C, V and O) present in the film. For R–T analysis, a custom four-point probe station was used to measure the resistivity as a function of temperature. The distance between consecutive probes was approximately 2 mm, and depending on the resistance offered by the film, input current ranging from 5 mA to 100 mA was used for a temperature range of 25 °C to 100 °C. The thickness of the films was measured using a Bruker DektakXT stylus profilometer.

Computational study

Quantum Espresso was used to perform DFT calculations within the generalized gradient approximation of the revised Perdew–Burke–Ernzerhof (PBEsol).[28–31] Projector augmented wave (PAW) pseudopotentials parameterized for PBEsol with 13 valence electrons for V and 6 valence electrons for O were used.[32,33] Because of the strong Coulomb repulsion among the V 3d electrons, the PBE+U method was used for the calculations.[34] Setting the effective parameters, i.e., $U_{eff} = U - J$, where U is the Hubbard parameter and J is the screened exchange parameter, accurately describes the electronic structure and strong correlation of VO$_2$.[35–37] Values of U and J were chosen to be 4.2 eV and 0.8 eV, respectively, resulting in a U_{eff} of 3.4 eV, identical to those used by Yao et al.[35] The electron density and wavefunctions were expanded in plane waves with energy cutoffs of 560 and 70 Ry, respectively. Fermi–Dirac smearing with a Gaussian spreading of 0.001 Ry was used. Gamma-centered 5 × 6 × 5 and 6 × 6 × 5 k-meshes for sampling the reciprocal space were used for monoclinic and rutile phases, respectively. We used a 10^{-6} Ry energy difference as a convergence criterion for electronic relaxation. Atomic positions were relaxed until the force on every atom was less than 10^{-5} Ry bohr^{-1}. All calculations were spin-polarized to accurately describe the magnetic properties of VO$_2$.

We studied 12 atom supercells (4 V and 8 O) of monoclinic (M$_1$) (1 × 1 × 1) and rutile (R) (1 × 1 × 2) phases. The initial cell parameters of M$_1$ and R were used as: M$_1 \rightarrow a = 5.75$ Å, $b =$

4.53 nm, $c = 5.38$ nm, $\alpha = \gamma = 90°$, $\beta = 122.6°$ and R $\rightarrow a = b = 4.55$ nm, $c = 5.90$ nm, $\alpha = \beta = \gamma = 90°$. These cell parameters are consistent with the experimental study by Moatti et al.[38] Starting from these structures, we performed a full relaxation via energy minimization with respect to atomic positions, cell shape, and cell volume. To mimic the effect of the sapphire substrate, we applied the in-plane strain on the x–z plane of both monoclinic and rutile phases. We used the value of misfit strains measured by Moatti et al. experimentally, i.e., −4.42% and +2.27% along (100) and (001), respectively, and $\beta = 120°$ for the M$_1$ phase; +3.36% and −3.37% along (100) and (001), respectively, keeping all the angles at 90° for the R phase.[38] The out-of-plane cell parameter along (010) and atomic positions were relaxed to minimize energy.

Results and discussion

All the VO$_2$ thin film samples were deposited using PLD (see the Methodology). Fig. 1(a) shows the schematic of the lattice plane matching of VO$_2$ and c-Al$_2$O$_3$ involved in the film. The epitaxy relation was confirmed using XRD (discussed later). The [001] direction of VO$_2$ on the (020) interface has a domain-matching relationship with the (0006) face of c-cut sapphire, along the [1$\bar{1}$00] direction. The lattice parameter of VO$_2$ in the (020) plane along its c-plane i.e. [001] direction is 5.38 Å, while that for (0006) c-Al$_2$O$_3$ in the [1$\bar{1}$00] direction is 8.25 Å, hence forming an approximately 3 : 2 relationship, as shown in Fig. 1(b).[39,40] VO$_2$ also achieves domain matching with (0001) Al$_2$O$_3$ along the a-axis i.e. [100] direction, as it is in an approximately 10 : 7 ratio, along the [01$\bar{1}$0] direction of the (0001) sapphire face, as shown in Fig. 1(c).[39,40] A schematic of the VO$_2$ thin film stack is shown in Fig. 1(d).

To confirm the above epitaxy relationship, XRD was performed. Fig. 2(a) and (b) show the XRD plots of the VO$_2$ films deposited on (0001) Al$_2$O$_3$. While Fig. 2(a) is a comparison of films deposited at 5 mTorr oxygen chamber pressure at 550 °C, 600 °C, and 650 °C substrate temperatures, Fig. 2(b) is a comparison of VO$_2$ deposited at three different oxygen pressures of 2.5 mTorr, 5 mTorr and 7.5 mTorr, with the substrate temperature during deposition for all three films being 600 °C. The XRD θ–2θ scans of the VO$_2$ thin films confirm the highly textured growth of VO$_2$ along the (020) out-of-plane for all cases with compressive strain present along the out-of-plane direction, indicative of the in-plane tensile strain (2θ value for bulk M$_1$-VO$_2$ (020) = 39.68°). The data shows that with increasing deposition temperatures, the FWHM of the VO$_2$ samples decreases, while the d-spacing increases, leading to a decrease in the compressive strain from −0.71% to −0.44% as shown in Fig. 2(d). This is due to the increase in the film crystallinity as the deposition temperature increases, along with a continuous reduction in compressive strain along the b-axis.[41] With respect to oxygen partial pressure during deposition, the compressive strain along the b-axis is minimum at −0.48% for the sample deposited at 5 mTorr, while it increases to −0.93% and −0.97% for samples deposited at 2.5 mTorr and 7.5 mTorr oxygen pressure as shown in Fig. 2(c). This may be due to the three-dimensional nature of the V–O bond, as extension of the
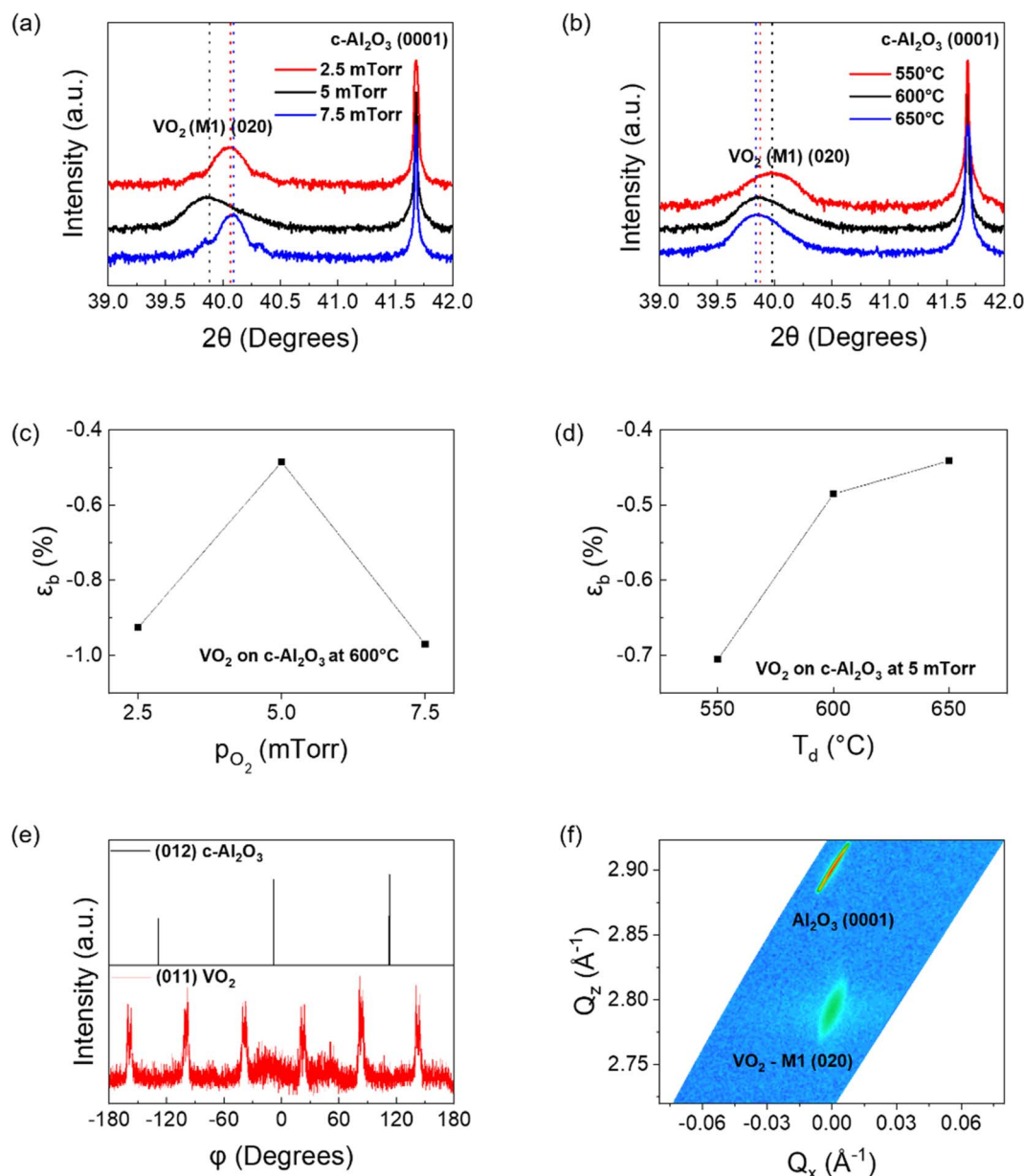
Fig. 2 XRD analysis of the VO_2 samples – the temperature-wise comparisons for VO_2 films deposited at 5 mTorr oxygen pressure (a), the changes in the XRD scans with respect to oxygen pressure keeping the deposition substrate temperature constant at 600 °C (b), and the respective strains calculated (c and d). φ scan results confirming the epitaxial nature of the VO_2 film (e), and the RSM plot of the VO_2 film deposited at 5 mTorr oxygen pressure and 600 °C substrate temperature (f).

lattice parameter along the out-of-plane b-axis usually leads to compression along the other two axes, and *vice versa*, owing to the lattice distortion by oxygen vacancies (discussed later).[42] The non-linear effects of increasing oxygen content in the chamber have been reported earlier.[24] In summary, due to the three-dimensional nature of V–O bonds, since compression in one direction leads to stretching along the other two, there is a possibility that the VO_2 film has an optimal zone of minimum compressive strain along the b-axis with respect to the *in situ* oxygen partial pressure. Any change in oxygen pressure from 5 mTorr will increase the out-of-plane compressive strain in the film.

Phi (φ) scans of the 5 mTorr sample, deposited at 600 °C, are shown in Fig. 2(e). Here, the φ scan of the (012) plane (also called r-plane) of sapphire ($2\theta = 25.56°$; $\psi = 57.7°$) showed three-fold symmetry, each peak spaced 120° apart, confirming the three-fold symmetry of the trigonal substrate. φ scans of VO_2 for the (011) plane ($2\theta = 27.87°$; $\psi = 44.9°$) confirmed the two-fold symmetry of monoclinic VO_2 on each of the three r-planes, thus giving six peaks in φ scan.[38,43] The (011) VO_2 scans demonstrated 30° rotation with respect to the $[1\bar{1}02]$ sapphire axis, which matches well with earlier reports.[38] The (020) as well as (002) peaks of VO_2 have approximately the same d-spacing (2.27 Å), as well as similar tilts with respect to the (011) plane (45° and 44.9°). Hence, the out-of-plane XRD results cannot

confirm on their own if the VO$_2$ peaks obtained in this setup are from (020) or (002) orientation. To clarify further on this issue, the φ scans for the (110) peak with respect to (020) and (002) out of plane VO$_2$ orientations are shown in ESI Fig. S1.† The (110) orientation for VO$_2$ has Bragg angle $2\theta = 26.92°$, with its tilt with respect to the (020) and (002) planes being $\psi_{(020)} = 43.1°$ and $\psi_{(002)} = 68.4°$ respectively. Fig. S1(a)† confirms the (020) out-of-plane orientation for the VO$_2$ film grown on (0001) sapphire, as the other configuration yields a much poorer XRD plot, as shown in Fig. S1(b).† Moatti *et al.* have shown the critical thickness for VO$_2$ grown on *c*-sapphire with an NiO buffer layer to be approximately 15 nm, while all of the films grown in this study were determined by the profilometer to be approximately 50 nm.[44] This is also confirmed by the study of Moatti *et al.*, in which they showed that VO$_2$ films grown epitaxially on *c*-Al$_2$O$_3$ substrates grow with (200) and (020) out of plane grown for

thickness below and above the critical limit respectively.[45] Han *et al.* have reported the critical thickness of an epitaxial VO$_2$ thin film on *c*-sapphire to be approximately 4 nm.[46] The (020) orientation growth observed in the VO$_2$ films grown thus confirms that films have thickness above the critical limit. Reciprocal Space Mapping (RSM) of the VO$_2$ film deposited at 5 mTorr oxygen pressure and 600 °C is shown in Fig. 2(f), which confirms the epitaxial nature of the film. The film shows a very small spread in the reciprocal axis ($\Delta Q_x = 0.02$ Å^{-1} along Q_x and $\Delta Q_z = 0.5$ Å^{-1} along Q_z) confirming the high quality of the film. A larger spread is associated with more defects, such as edge dislocations and grain boundaries, and therefore likely to be nucleation sites for other phases, such as M$_2$.[47] From these ΔQ_x and ΔQ_z values, the in-plane and out-of-plane correlation length can be calculated as $d_{ip} = 2\pi/\Delta Q_x$ and $d_{op} = 2\pi/\Delta Q_z$ respectively. The d_{ip} and d_{op} have been calculated to be 31.4 nm and
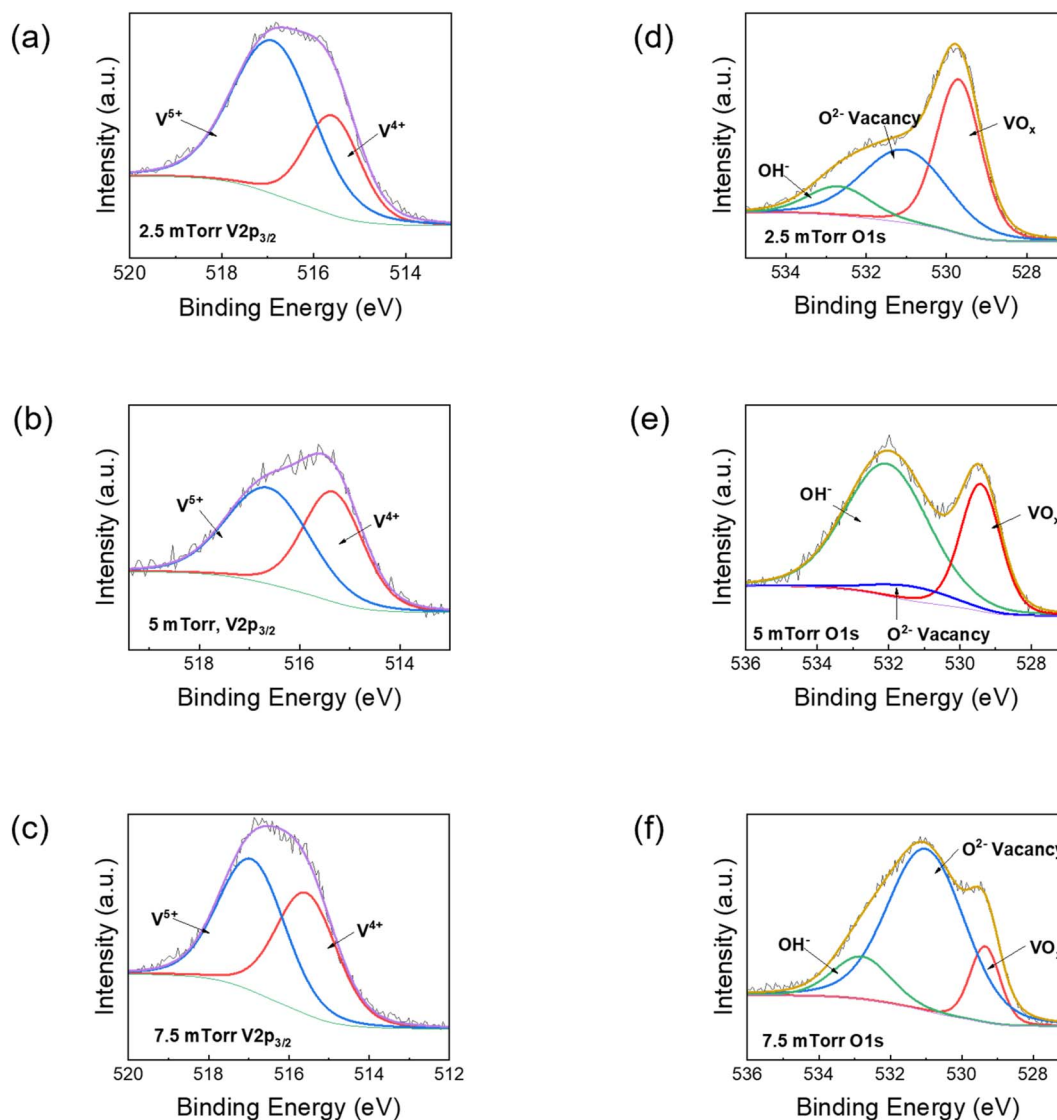

Fig. 3 XPS plots of the VO$_2$ samples deposited on (0001) Al$_2$O$_3$ – (a, b and c) the de-convolution of V 2p peaks for VO$_2$ films formed at varying oxygen pressure levels (substrate temperature being 600 °C), and (d, e and f) the de-convoluted XPS data points of the O 1s level corresponding to the V 2p peaks in (a), (b) and (c) respectively.

1.26 nm respectively. d_{ip} being much larger than d_{op} is indicative of in-plane nucleation of VO_2 being the dominant factor, rather than layer-by-layer growth.[48,49]

Further, the effect of oxygen partial pressure on the oxygen vacancies was studied using XPS. Fig. 3 shows the XPS data, in which the de-convoluted peaks of the V $2p_{1/2}$, V $2p_{3/2}$ and O $1s_{1/2}$ for films deposited at 2.5 mTorr, 5 mTorr and 7.5 mTorr are presented. The de-convolution of V 2p peaks is explained in Fig. 3(a), (c) and (e), while the analysis of O 1s spectra is shown in Fig. 3(b), (d) and (f) for VO_2 films deposited at 2.5 mTorr, 5 mTorr and 7.5 mTorr respectively. The substrate temperature for all the films was 600 °C. The V $2p_{3/2}$ peaks are used for comparison. The V $2p_{3/2}$ peak is de-convoluted into two peaks for every sample, centred at 515.6 eV (corresponding to V^{4+}) and 516.8 eV (corresponding to V^{5+}), with the values matching with the literature.[24,50,51] The XPS results did not validate the presence of any V^{3+} ions. The lack of any V_2O_3 peaks in XRD results can be used in conjunction as evidence that V_2O_3 did not play any role in the SMT analysis of the VO_2 films. The results in Fig. 3(a), (c) and (e) show the lowest V^{4+} content for the VO_2 film formed at 2.5 mTorr partial oxygen pressure (30.54%), while higher values of V^{4+} at 45.28% and 45.83% are observed at oxygen pressures of 5 mTorr and 7.5 mTorr respectively. This might be due to overaccumulation of O^{2-} ions on the substrate surface, which results in a smaller number of oxygen ions being able to diffuse into the film and both with vanadium ions, a phenomenon observed in previous reports.[23,24] It also explains why the VO_2 samples deposited at 5 mTorr and 7.5 mTorr oxygen pressure have higher switching ratios in the resistivity *vs.* temperature plots, as it is VO_2 that is primarily responsible for the metal-to-insulator transition (discussed later). The binding energy of V^{4+} for the VO_2 fabricated at 5 mTorr is also the lowest among the three (515.33 eV), which suggests increased electronegativity compared to the other films (515.59 eV for 2.5 mTorr and 515.56 eV for 7.5 mTorr respectively). In the case of the O 1s peak, the one attributed to VO_x bonding at 529.42 ± 0.2 eV has the highest percentage for the film fabricated at 2.5 mTorr, shown in Fig. 3(b), while it decreases with increases in oxygen pressure. However, in the case of a film fabricated at 2.5 mTorr, fewer V^{4+} ions are available compared to V^{5+} for bonding with O^{2-}, while in the case of 7.5 mTorr oxygen pressure, the VO_x content within the sample is the lowest, both in terms of intensity as well as percentage. Hence, it is plausible that the VO_2 content is best formed in the film fabricated at 5 mTorr oxygen pressure.

To further understand the effect of temperature and oxygen partial pressure on the VO_2 film quality, Raman spectroscopy was performed. The peaks in Raman spectroscopy plots are categorized as per the wave number at which they're located (<400 cm^{-1} for V–O–V bending spectra, 400 to 800 cm^{-1} for V–O–V stretching mode and >800 cm^{-1} for V=O stretching mode),[52] with the Raman peak at 192 cm^{-1} being also attributed to V–V twisting vibrations.[53,54] For both V–O and V–V peaks, it is seen that the shift to higher frequencies is highest for the VO_2 film deposited at 600 °C as shown in Fig. 4(a). This indicates that the lattice parameter stretching for the sample deposited at 600 °C is the lowest. A smaller V–O bond length should drive up

the transition temperature, since it makes it difficult for free electrons to be available for conduction. This correlates with the R–T results (discussed later), in which the transition temperature for the 600 °C VO_2 sample is the highest. However, a shorter V–V bond should reduce the transition temperature. Since for the film deposited at 600 °C, both the V–V as well as V–O bonds are the smallest, it suggests that the entire cell shrinks at certain deposition parameters, with the competition between V–O and V–V bonds determining whether the MIT increases or decreases. XRD plots indicate increasing relaxation along the b-axis with increasing deposition temperatures. From these three results, it can be understood that for lower deposition temperatures (550 °C and 600 °C), increasing deposition temperatures initiates b-axis relaxation as well as contraction along the in-plane axes. But for deposition at 650 °C, the VO_6 cell expands in all directions. Comparing between VO_2 films deposited at different oxygen pressures (substrate temperature for all of them being 600 °C), the trend in Fig. 4(b) is the opposite. The stretching frequency for the 5 mTorr VO_2 film is the lowest in both V–O and V–V bonds, indicating larger bond length for VO_2 deposited at 5 mTorr.[53] This is probably due to the lowest out-of-plane compressive strain for the 5 mTorr film, compared to the other films. Here, the peak corresponding to the V–O as well as V–V stretching shifts to higher frequency (*i.e.* lower bond length) for 2.5 mTorr as well 7.5 mTorr VO_2 samples as shown in Fig. 4(d). This means that the entire cell shrinks for films deposited at 2.5 mTorr as well as 7.5 mTorr oxygen pressure, with maximum cell volume for VO_2 films deposited at 5 mTorr in oxygen pressure-wise comparison. Moatti *et al.* have suggested that increasing vacancy leads to densification of the VO_2 lattice.[55] But the sudden shrinking of the lattice parameters at higher oxygen pressure (7.5 mTorr) suggests the relationship is not linear, since the trend of increasing MIT with increasing oxygen pressure continues to hold (discussed later) despite non-linear XRD and Raman trends. The FWHM comparison from Fig. 4(c)–(f) shows a minimum value for the VO_2 film deposited at 5 mTorr and 600 °C in oxygen pressure-wise comparison (for both V–V and V–O bonds), indicating that VO_2 films formed at this pressure are of better quality. However, the substrate temperature-wise comparison shows a further drop in FWHM at 650 °C, since higher deposition temperature leads to a more refined crystallinity. The signal-to-noise ratio for all the VO_2 attributed peaks was also the highest for the film deposited at 5 mTorr, further validating the observation that optimal VO_2 films on (0001) Al_2O_3 are formed at 5 mTorr oxygen pressure and 600 °C substrate temperature. The reflectivity analysis performed for the VO_2 films grown at 5 mTorr oxygen pressure, with varying substrate temperature is shown in ESI Fig. S2.† From the plots, we obtained the direct band gap values for the films grown at 550 °C, 600 °C and 650 °C substrate temperatures to be respectively 0.64 eV, 0.82 eV and 0.78 eV respectively. These are all close to the direct band gap for bulk VO_2 as reported in the literature.[5,10] These values also match with the T_c values obtained, which have been discussed later. Larger T_c implies an unstable metallic rutile phase, which should correspond to a larger band gap value, and *vice versa*. The Kubelka–
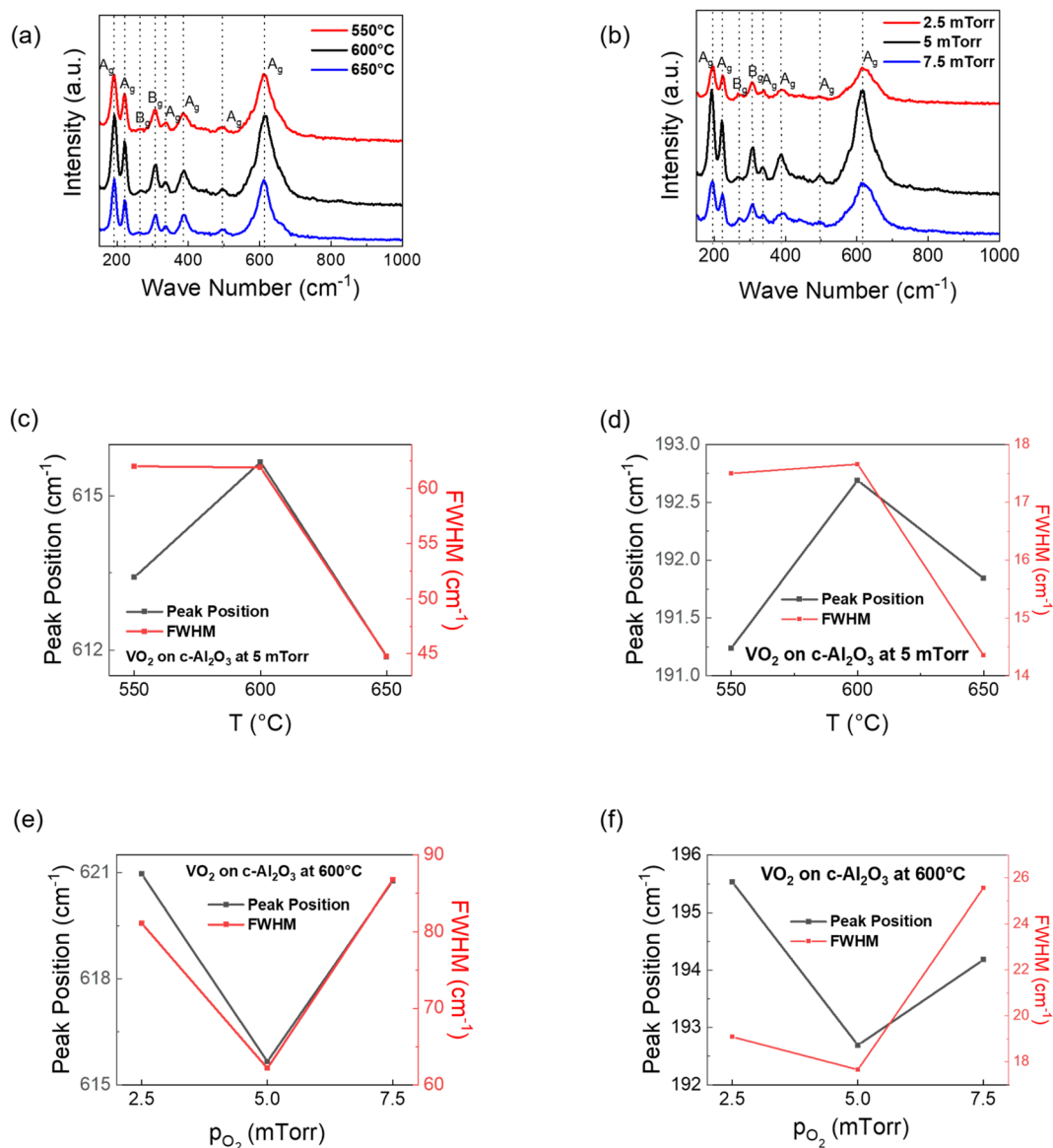
Fig. 4 Raman analysis of the VO$_2$ samples – (a) the Raman analysis of the substrate temperature-wise, and (b) the variation in Raman plot with change in oxygen pressure during deposition; (c and d) the respective FWHM and position of the main V–O and V–V stretching peaks with respect to deposition temperature respectively, and (e and f) oxygen pressure-wise comparison for the V–O and V–V peaks respectively.

Munk model was used for this analysis, as reported in the literature.[56]

Finally, the phase transition in VO$_2$ thin films was studied by measuring the resistivity of the film as a function of temperature using a custom four-point-probe setup. The resistivity *vs.* temperature (R–T) plots of the VO$_2$ samples are shown in Fig. 5. The heating and cooling curves for each sample have been indicated by arrows. The T_c for each sample was calculated by Gaussian fitting (not shown here) of both the logarithmic differential curves (heating and cooling) in Fig. 5(e) and (f), followed by averaging the value of both the troughs. All the plots show good switching (3 orders or more) with transition temperature greater than the 68 °C value of bulk VO$_2$. From Fig. 5(a), it is seen that the switching ratio reaches a maximum of 2 × 10^{-4} for the VO$_2$ film deposited at 600 °C substrate

temperature, while it reduces to 1.9 × 10^{-3} and 1.2 × 10^{-3} for VO$_2$ films deposited at 550 °C and 650 °C respectively. Overall, the results match well with the inferences derived from XRD, XPS and Raman spectroscopy discussions in previous sections. This can possibly indicate a reduction in quality of the VO$_2$ formed for substrate temperatures other than 600 °C. From the XRD plots, it should be presumed that the transition temperature should be highest for the VO$_2$ film deposited at 550 °C, since it has the highest out-of-plane compressive strain. However, that is not the case. In fact, the 550 °C sample has lower transition temperature (65.06 °C) compared to the VO$_2$ film deposited at 600 °C (75.26 °C), as shown in Fig. 5(e). This could be explained by competition between different axial strains as well as the changes in V–O bond length alongside V–V bond length, as explained in the previous section. While the
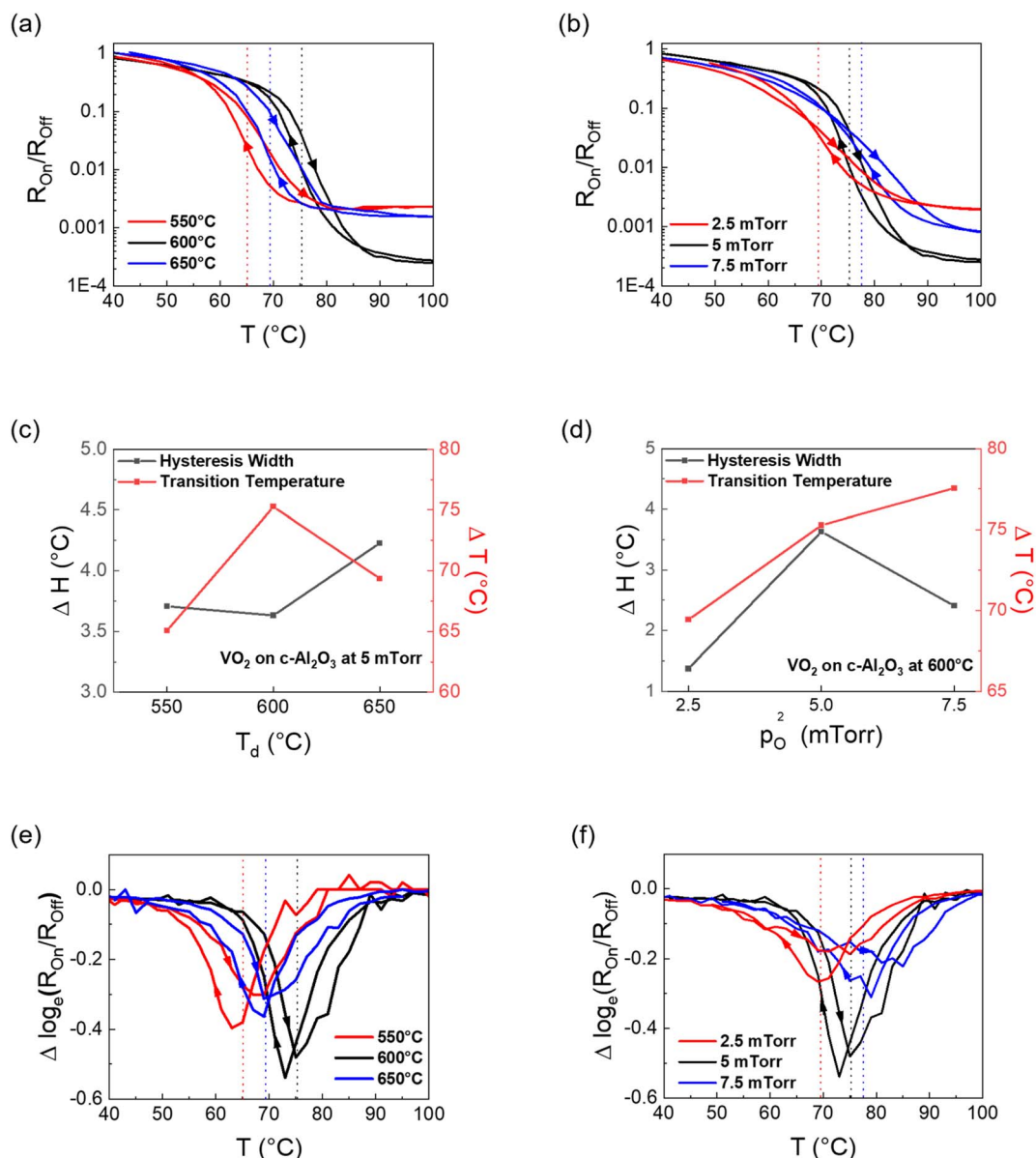
Fig. 5 Resistivity analysis of the VO$_2$ on c-cut sapphire as a function of temperature – (a) the comparison between three VO$_2$ films deposited at 550 °C, 600 °C and 650 °C substrate temperatures, with the oxygen pressure constant at 5 mTorr, (b) the R–T comparisons for the three films with varying oxygen pressures of 2.5 mTorr, 5 mTorr and 7.5 mTorr, with the substrate temperature being kept constant at 600 °C in all of them, (c and d) their corresponding ΔH and T_c analysis; (e and f) the differential plots of the results in (a) and (b), from which T_c is calculated (heating and cooling curves in all the plots are indicated by arrows and the T_c for each sample is shown by a vertical dashed line).

interplanar spacing along the b-axis increases with increasing substrate deposition temperature, as shown by the XRD plots in Fig. 2(a), it also means that the lattice parameter along the other two axes should reduce. Hence, for VO$_2$ films formed at 650 °C, it is possible that the V–O bond length expansion overcompensates for the V–V bond length expansion, thus causing the T_c to reduce again. The hysteresis width comparison for the three samples is given in Fig. 5(c). The difference between the heating and cooling curves is the smallest for the VO$_2$ film deposited at 600 °C. Compared with higher switching amplitude, it indicates higher film quality and lower grain boundary density translating to lower interfacial energy.[19] Fig. 5(b) and (d)

compare the R–T results with a change in oxygen partial pressure during deposition, where all the VO$_2$ films were deposited at 600 °C. Clearly, the T_c reduces with the reduction in oxygen partial pressure during deposition (69.4 °C for 2.5 mTorr, 75.3 °C for 5 mTorr and 77.6 °C for 7.5 mTorr), as shown by the differential plots in Fig. 5(f). The increasing T_c with a corresponding increase in oxygen pressure can be attributed to oxygen vacancies, since oxygen vacancies act as conducting channels and help to stabilize the metallic tetragonal phase of VO$_2$.[23] The hysteresis width for the film deposited at 600 °C, however, is the highest when compared across oxygen partial pressures. Compressive strain along the c-axis is associated with

Table 1 Lattice parameters and the energetics of the bulk and strained monoclinic (M_1) and rutile (R) phases. The energy of the M_1 phase is used as a reference for both bulk and strained cases. The in-plane lattice parameters (a, c, and β) for the strained case correspond to the experimental values for the sapphire substrate. The out-of-plane lattice parameters (b) are fully relaxed

	Phase	a (Å)	b (Å)	c (Å)	α (°)	β (°)	γ (°)	$E - E_{M_1}$ (meV per VO_2)
Bulk	M_1	6.01	4.43	5.36	90	124.12	90	0
	R	4.54	4.54	5.71	90	90	90	82.1
Strained	M_1	5.74	4.35	5.48	90	120	90	0
	R	4.69	4.49	5.51	90	90	90	118.8

a reduction in MIT owing to the stabilization of the denser, high-temperature metallic phase.[41] Since the XRD results in this case show compressive strain along the b-axis, DFT calculations were done to understand the strain effect on the phase stability.

Table 1 summarizes the lattice parameters and the energetics of the bulk and strained M_1 & R phases. Our relaxed parameters for bulk VO_2 are within 4% of experimental lattice parameters which is typical in DFT calculations. Our calculations reveal the energy difference between the high temperature R and low temperature M_1 phases to be 82.1 meV per VO_2 at 0 K.

We find that the in-plane strains on M_1 mimic the sapphire substrate, resulting in −1.98% strain along the out-of-plane direction (010) as compared to the bulk M_1 phase.[38] The value for this out-of-plane strain on the R phase is found to be −1.03%, which is lower and consistent with the experimental results in this study. Moreover, the in-plane strains associated with the sapphire substrate increase the 0 K energy difference between R and M_1 phases to 118.8 meV per VO_2, which corresponds to higher stability of the M_1 phase at 0 K and higher M_1 → R transformation temperatures.[38] We find similar behaviour
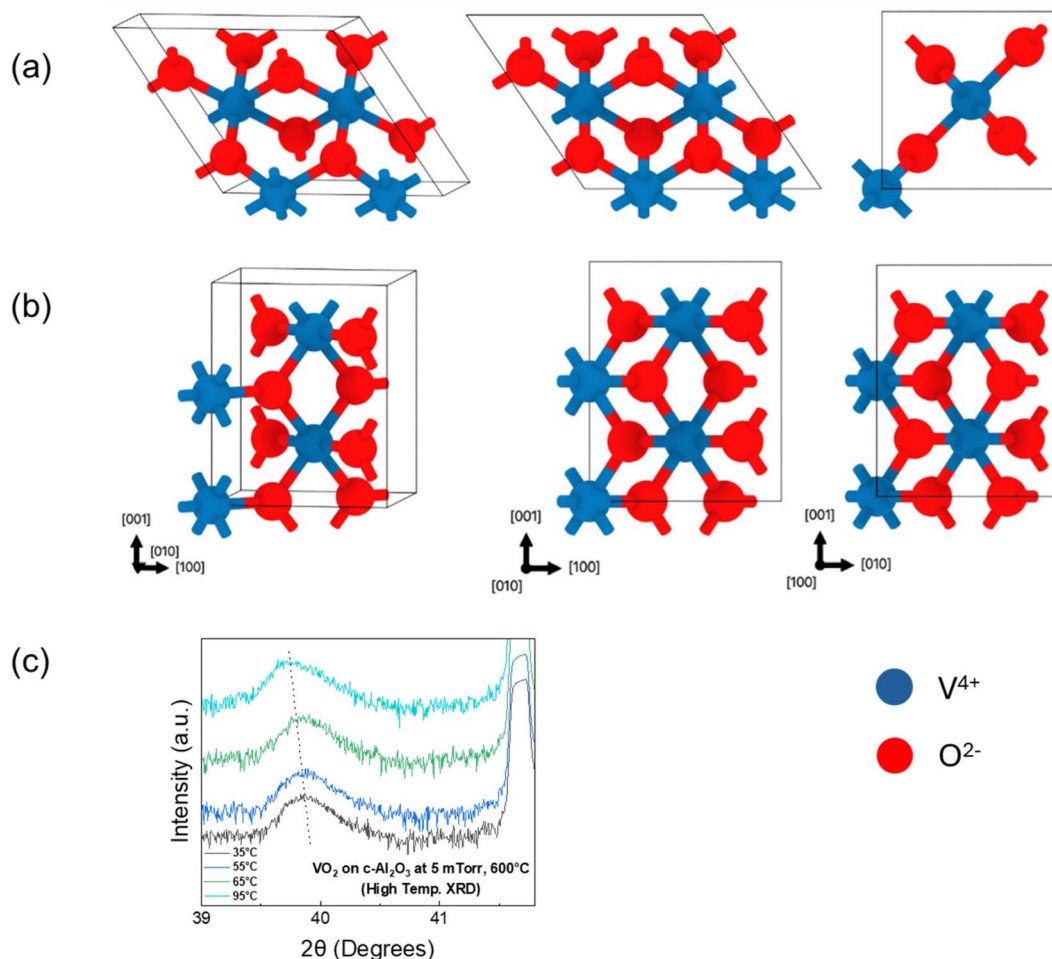

Fig. 6 Schematic of the VO_2 in bulk mode for (a) monoclinic and (b) tetragonal phases, and (c) the corresponding experimental results of high temperature X-ray diffraction, with the shift in the 2θ value confirming the transition at high temperatures.

experimentally where the deposition of the VO_2 thin film on the sapphire substrate increases the transformation temperature as compared to the bulk VO_2. In experiments, n unit cells of the substrate can match with m unit cells of the film to minimize the epitaxial strain. We note that we are using an upper limit where $n = m$, which provides the upper bound. The experimental strain will be some fraction n/m, impacting the quantitative predictions (which will lie in between our bulk and strained calculation). However, the qualitative picture and two main conclusions will remain the same: (i) the presence of substrate results in lower out-of-plane strain in the R phase compared to M_1 and (ii) the c-Al_2O_3 substrate stabilizes the M_1 phase and will lead to higher transformation temperature. Fig. 6(a) and (b) show the relaxed structures of the bulk VO_2 for monoclinic and tetragonal phases. At higher temperatures, VO_2 retains its (020) out-of-plane orientation, but it is characterized by a reduction in d-spacing. High-temperature XRD was performed for the VO_2 film deposited at 5 mTorr oxygen pressure and 600 °C substrate temperature, the results of which are plotted in Fig. 6(c). At 35 °C, the film has a d-spacing of 2.258 Å ($2\theta = 39.87°$), which shifts to a d-spacing of 2.264 Å ($2\theta = 39.76°$), when heated up to temperatures at which complete transition from the monoclinic M_1 (020) to tetragonal T (020) phase has occurred, which is consistent with the DFT calculations.

Conclusion

In this work, we successfully fabricated epitaxial VO_2 thin films on c-Al_2O_3 substrates by the pulsed laser deposition technique. T_c tuning was achieved by varying the two main parameters of deposition – substrate temperature and partial pressure of oxygen during deposition. The epitaxial nature of VO_2 films was confirmed by XRD scans, while Raman spectroscopy identified the various phonon modes associated with VO_2. The XPS scans confirmed the C, V and O contents in the sample, and described the changing of quantity of each element due to varying the deposition parameters. The R–T results showed maximum switching for the VO_2 film deposited at 600 °C substrate temperature and 5 mTorr oxygen pressure, with high switching unlocking potential for its use in memristive devices. DFT calculations supported the experimental findings. Our study provides a better understanding of the interplay between strain and oxygen vacancies and their effect on the physical properties of VO_2 thin films.

Data availability

The data supporting the findings presented in this study are not publicly available at this time, but may be obtained from the corresponding author upon reasonable request.

Conflicts of interest

There are no conflicts to declare.

References

1 R. Xie, C. T. Bui, B. Varghese, Q. Zhang, C. H. Sow, B. Li and J. T. L. Thong, *Adv. Funct. Mater.*, 2011, **21**, 1602–1607.
2 S. Lee, C. Cheng, H. Guo, K. Hippalgaonkar, K. Wang, J. Suh, K. Liu and J. Wu, *J. Am. Chem. Soc.*, 2013, **135**, 4850–4855.
3 B. Hu, Y. Ding, W. Chen, D. Kulkarni, Y. Shen, V. V. Tsukruk and Z. L. Wang, *Adv. Mater.*, 2010, **22**, 5134–5139.
4 E. Strelcov, A. Tselev, I. Ivanov, J. D. Budai, J. Zhang, J. Z. Tischler, I. Kravchenko, S. V. Kalinin and A. Kolmakov, *Nano Lett.*, 2012, **12**, 6198–6205.
5 Z. Shao, X. Cao, H. Luo and P. Jin, *NPG Asia Mater.*, 2018, **10**, 581–605.
6 S. H. Bae, S. Lee, H. Koo, L. Lin, B. H. Jo, C. Park and Z. L. Wang, *Adv. Mater.*, 2013, **25**, 5098–5103.
7 Z. Khan, P. Singh, S. A. Ansari, S. R. Manippady, A. Jaiswal and M. Saxena, *Small*, 2021, **17**(4), e2006651.
8 P. Schofield, A. Bradicich, R. M. Gurrola, Y. Zhang, T. D. Brown, M. Pharr, P. J. Shamberger and S. Banerjee, *Adv. Mater.*, 2023, **35**, 2205294.
9 Y. Yang, X. Mao, Y. Yao, H. Huang, Y. Lu, L. Luo, X. Zhang, G. Yin, T. Yang and X. Gao, *J. Appl. Phys.*, 2019, **125**, 082508.
10 W. K. Hong, S. Cha, J. I. Sohn and J. M. Kim, *J. Nanomater.*, 2015, 538954.
11 J. D. Budai, A. Tselev, J. Z. Tischler, E. Strelcov, A. Kolmakov, W. J. Liu, A. Gupta and J. Narayan, *Acta Mater.*, 2013, **61**, 2751–2762.
12 K. Liu, S. Lee, S. Yang, O. Delaire and J. Wu, *Mater. Today*, 2018, **21**, 875–896.
13 X. Gao, C. M. M. Rosário and H. Hilgenkamp, *AIP Adv.*, 2022, **12**, 015218.
14 M. Samizadeh Nikoo, R. Soleimanzadeh, A. Krammer, G. Migliato Marega, Y. Park, J. Son, A. Schueler, A. Kis, P. J. W. Moll and E. Matioli, *Nature Electronics*, 2022, **5**, 596–603.
15 Y. Yang, L. Wang, H. Huang, C. Kang, H. Zong, C. Zou, Y. Lu, X. Li, B. Hong and C. Gao, *Ceram. Int.*, 2018, **44**, 3348–3355.
16 T. H. Yang, R. Aggarwal, A. Gupta, H. Zhou, R. J. Narayan and J. Narayan, *J. Appl. Phys.*, 2010, **107**, 053514.
17 J. Jian, X. Wang, S. Misra, X. Sun, Z. Qi, X. Gao, J. Sun, A. Donohue, D. G. Lin, V. Pol, J. Youngblood, H. Wang, L. Li, J. Huang and H. Wang, *Adv. Funct. Mater.*, 2019, **29**, 1903690.
18 Z. He, J. Jian, S. Misra, X. Gao, X. Wang, Z. Qi, B. Yang, D. Zhang, X. Zhang and H. Wang, *Nanoscale*, 2020, **12**, 17886–17894.
19 Z. He, J. Jian, L. Quigley, N. A. Bhatt, J. P. Barnard, C. A. Mihalko, H. Wang, X. L. Phuah, J. Lu, X. Xu and H. Wang, *Adv. Phys. Res.*, 2023, **2**, 2300031.
20 K. Mulchandani, A. Soni, K. Pathy and K. R. Mavani, *Superlattices Microstruct.*, 2021, **154**, 106883.
21 Y. Yang, G. Wang, W. Huang, C. Wang, Y. Yao, X. Mao, H. Lin, T. Zhang, H. Qiu, Z. Li, H. Zhang, Y. Yin, J. Guo, Y. Guan, W. Yan, Z. Luo, C. Zou, Y. Tian, G. Xiao, X. Li and C. Gao, *Sci. China Mater.*, 2021, **64**, 1687–1702.
22 A. Moatti, R. Sachan and J. Narayan, *J. Appl. Phys.*, 2020, **128**, 045302.

23 S. Kittiwatanakul, J. Laverock, D. Newby, K. E. Smith, S. A. Wolf and J. Lu, *J. Appl. Phys.*, 2013, **114**, 053703.

24 S. A. Bukhari, S. Kumar, P. Kumar, S. P. Gumfekar, H. J. Chung, T. Thundat and A. Goswami, *Appl. Surf. Sci.*, 2020, **529**, 146995.

25 L. Fan, X. Wang, F. Wang, Q. Zhang, L. Zhu, Q. Meng, B. Wang, Z. Zhang and C. Zou, *RSC Adv.*, 2018, **8**, 19151–19156.

26 E. K. Koussi, F. Bourquard, T. Tite, D. Jamon, F. Garrelie and Y. Jourlin, *Appl. Surf. Sci.*, 2020, **521**, 146267.

27 W. Lu, L. M. Wong, S. Wang and K. Zeng, *Journal of Materiomics*, 2018, **4**, 360–367.

28 P. Giannozzi, O. Andreussi, T. Brumme, O. Bunau, M. Buongiorno Nardelli, M. Calandra, R. Car, C. Cavazzoni, D. Ceresoli, M. Cococcioni, N. Colonna, I. Carnimeo, A. Dal Corso, S. De Gironcoli, P. Delugas, R. A. Distasio, A. Ferretti, A. Floris, G. Fratesi, G. Fugallo, R. Gebauer, U. Gerstmann, F. Giustino, T. Gorni, J. Jia, M. Kawamura, H. Y. Ko, A. Kokalj, E. Kücükbenli, M. Lazzeri, M. Marsili, N. Marzari, F. Mauri, N. L. Nguyen, H. V. Nguyen, A. Otero-De-La-Roza, L. Paulatto, S. Poncé, D. Rocca, R. Sabatini, B. Santra, M. Schlipf, A. P. Seitsonen, A. Smogunov, I. Timrov, T. Thonhauser, P. Umari, N. Vast, X. Wu and S. Baroni, *J. Phys.: Condens. Matter*, 2017, **29**, 465901.

29 P. Giannozzi, S. Baroni, N. Bonini, M. Calandra, R. Car, C. Cavazzoni, D. Ceresoli, G. L. Chiarotti, M. Cococcioni, I. Dabo, A. Dal Corso, S. De Gironcoli, S. Fabris, G. Fratesi, R. Gebauer, U. Gerstmann, C. Gougoussis, A. Kokalj, M. Lazzeri, L. Martin-Samos, N. Marzari, F. Mauri, R. Mazzarello, S. Paolini, A. Pasquarello, L. Paulatto, C. Sbraccia, S. Scandolo, G. Sclauzero, A. P. Seitsonen, A. Smogunov, P. Umari and R. M. Wentzcovitch, *J. Phys.: Condens. Matter*, 2009, **21**, 395502.

30 P. Giannozzi, O. Baseggio, P. Bonfà, D. Brunato, R. Car, I. Carnimeo, C. Cavazzoni, S. De Gironcoli, P. Delugas, F. Ferrari Ruffino, A. Ferretti, N. Marzari, I. Timrov, A. Urru and S. Baroni, *J. Chem. Phys.*, 2020, **152**(15), 154105.

31 J. P. Perdew, A. Ruzsinszky, G. I. Csonka, O. A. Vydrov, G. E. Scuseria, L. A. Constantin, X. Zhou and K. Burke, *Phys. Rev. Lett.*, 2008, **100**, 136406.

32 P. E. Blochl, *Phys. Rev. B: Condens. Matter Mater. Phys.*, 1994, **50**, 17953.

33 G. Kresse and D. Joubert, *Phys. Rev. B: Condens. Matter Mater. Phys.*, 1999, **59**, 1758.

34 S. L. Dudarev, G. A. Botton, S. Y. Savrasov, C. J. Humphreys and A. P. Sutton, *Phys. Rev. B: Condens. Matter Mater. Phys.*, 1998, **57**, 1505.

35 T. Yao, X. Zhang, Z. Sun, S. Liu, Y. Huang, Y. Xie, C. Wu, X. Yuan, W. Zhang, Z. Wu, G. Pan, F. Hu, L. Wu, Q. Liu and S. Wei, *Phys. Rev. Lett.*, 2010, **105**, 226405.

36 J. Wei, H. Ji, W. Guo, A. H. Nevidomskyy and D. Natelson, *Nat. Nanotechnol.*, 2012, **7**, 357–362.

37 Y. Cui, S. Shi, L. Chen, H. Luo and Y. Gao, *Phys. Chem. Chem. Phys.*, 2015, **17**, 20998–21004.

38 A. Moatti, R. Sachan, J. Prater and J. Narayan, *ACS Appl. Mater. Interfaces*, 2017, **9**, 24298–24307.

39 A. Ainabayev, D. Mullarkey, B. Walls, D. Caffrey, K. Zhussupbekov, A. Zhussupbekova, C. Ilhan, A. Kaisha, P. Biswas, A. Tikhonov, O. Murtagh and I. Shvets, *ACS Appl. Nano Mater.*, 2023, **6**, 2917–2927.

40 J. Jian, A. Chen, Y. Chen, X. Zhang and H. Wang, *Appl. Phys. Lett.*, 2017, **111**, 153102.

41 S. A. Howard, E. Evlyukhin, G. Páez Fajardo, H. Paik, D. G. Schlom and L. F. J. Piper, *Adv. Mater. Interfaces*, 2021, **8**, 2001790.

42 C. Zhang, G. Liu, X. Geng, K. Wu and M. Debliquy, *Sens. Actuators, A*, 2020, **309**, 112026.

43 L. Diebold, T. Maroutian, L. Largeau, N. Guiblin, R. Bude, G. Garry, O. M. Ishchenko and P. Aubert, *Appl. Phys. Lett.*, 2023, **123**, 131601.

44 A. Moatti, R. Sachan and J. Narayan, *Mater. Res. Lett.*, 2020, **8**, 16–22.

45 A. Moatti, R. Sachan, V. R. Cooper and J. Narayan, *Sci. Rep.*, 2019, **9**, 3009.

46 K. Han, L. Wu, Y. Cao, H. Wang, C. Ye, K. Huang, M. Motapothula, H. Xing, X. Li, D.-C. Qi, X. Li and X. R. Wang, *ACS Appl. Mater. Interfaces*, 2021, **13**, 16688–16693.

47 Y. Ji, Y. Zhang, M. Gao, Z. Yuan, Y. Xia, C. Jin, B. Tao, C. Chen, Q. Jia and Y. Lin, *Sci. Rep.*, 2014, **4**, 4854.

48 E. Ekström, S. Hurand, A. le Febvrier, A. Elsukova, P. O. Å. Persson, B. Paul, F. Eriksson, G. Sharma, O. Voznyy, D. G. Sangiovanni, G. Ramanath and P. Eklund, *Mater. Des.*, 2023, **229**, 111864.

49 R. Yue, Y. Nie, L. A. Walsh, R. Addou, C. Liang, N. Lu, A. T. Barton, H. Zhu, Z. Che, D. Barrera, L. Cheng, P. R. Cha, Y. J. Chabal, J. W. P. Hsu, J. Kim, M. J. Kim, L. Colombo, R. M. Wallace, K. Cho and C. L. Hinkle, *2D Mater.*, 2017, **4**, 045019.

50 G. Silversmit, D. Depla, H. Poelman, G. B. Marin and R. De Gryse, *J. Electron Spectrosc. Relat. Phenom.*, 2004, **135**, 167–175.

51 M. J. Powell, I. J. Godfrey, R. Quesada-Cabrera, D. Malarde, D. Teixeira, H. Emerich, R. G. Palgrave, C. J. Carmalt, I. P. Parkin and G. Sankar, *J. Phys. Chem. C*, 2017, **121**, 20345–20352.

52 M. Taha, S. Walia, T. Ahmed, D. Headland, W. Withayachumnankul, S. Sriram and M. Bhaskaran, *Sci. Rep.*, 2017, **7**, 17899.

53 E. Evlyukhin, S. A. Howard, H. Paik, G. J. Paez, D. J. Gosztola, C. N. Singh, D. G. Schlom, W. C. Lee and L. F. J. Piper, *Nanoscale*, 2020, **12**, 18857–18863.

54 K. Okimura, N. Hanis Azhan, T. Hajiri, S. I. Kimura, M. Zaghrioui and J. Sakai, *J. Appl. Phys.*, 2014, **115**, 153501.

55 A. Moatti, R. Sachan, S. Gupta and J. Narayan, *ACS Appl. Mater. Interfaces*, 2019, **11**, 3547–3554.

56 K. Brajesh, S. Ranjan, R. Kumar, R. Gupta, A. Dixit and A. Garg, *J. Am. Ceram. Soc.*, 2023, **106**, 6769–6777.